

## **An Evolutionary Shaking-Forecast-Based Earthquake Early Warning Method**

Aldo Zollo, Simona Colombelli, Alessandro Caruso\* and Luca Elia

Department of Physics, University of Naples Federico II

\*now at RFI, Rete Ferroviaria Italiana, Rome

### **Abstract**

Here we propose a methodology for Earthquake Early Warning able to issue the alert based on the real-time estimation of the epicentral area where a peak ground Intensity measure is expected to exceed a user-set ground shaking level. The method provides in output a P-wave-based, time-evolutive “early” shake map. It combines the Peak Ground Velocity (PGV) predictions available from the observed P-wave amplitudes and from the region-specific Ground Motion Prediction Equation (GMPE), using progressively updated estimates of earthquake location and magnitude. The P-wave displacement, velocity and acceleration amplitudes are jointly measured on a progressively expanded P-wave time window while the earthquake location and magnitude are evaluated using the first P-arrival time and displacement amplitudes at near source stations. A retrospective analysis of the 2016, Mw 6.5 Central Italy earthquake records shows that depending on the network density and spatial source coverage, the method naturally accounts for effects related to the earthquake rupture directivity and spatial variability of strong ground motion related to crustal wave propagation and site amplification. Within 1.5 sec since the first alert (5.15 sec after the origin time), the simulated performance of the system in predicting the event ground

---

\* Now at RFI, Rete Ferroviaria Italiana, Rome

shaking is very high: in the 40 km-radius area that suffered an Intensity MCS VIII-IX, 41 over 42 strong-motion instrumented sites would have been successfully alerted, with only one false alarm. Even considering the calculated blind-zone of 15 km radius, a 15-55 km wide annular area would have received the alert 2-14.5 sec before the occurrence of the strong ground shaking. The proposed EEW method evolves with time in a way that it minimizes the missed alarms while increasing successful alarms and to a lesser extent false alarms, so it is necessary for the end-user to accept these possibilities and account for them in a probabilistic decision scheme depending on the specific safety actuation measure to be undertaken in real-time.

## **1. INTRODUCTION**

Earthquake Early Warning (EEW) systems are modern, real-time seismic monitoring infrastructures aimed at issuing an alert and activating emergency safety measures to protect people, buildings, and industrial facilities in advance to the impact of strong and potentially damaging shaking waves. The basic principle on which network-based EEW systems ground on, is to use the time lag between the alert message issuance and the arrival of damaging seismic waves, to broadcast an alert soon after the first P-waves are detected at a near-source deployed, seismic network. The early warning can reach seconds or tens of seconds in advance the sites to be protected against the arrival of strong shaking waves, depending on the travel distance from the source. Onsite or stand-alone early warning systems use a single station or small-aperture arrays of sensors deployed in proximity of the target site to secure. In this case, the measures of the initial P-wave amplitude and/or the dominant signal frequency can be used as proxies for the late arriving, strongest shaking wave amplitudes at the same site, with no need for information on the earthquake location and magnitude (*Wu and Kanamori [2005]*). Along this same research direction we mention , among others, the algorithm that has been developed to estimate the seismic intensity from real-time early P-wave signals (*Yamamoto et al., 2008*), the threshold-based method

that uses the time-domain measurement of the cumulative absolute velocity from strong motion records (Alcik et al., 2009) and the B-delta method that estimates the earthquake epicentral distance and magnitude from modelling the rise of the early P-wave amplitude envelope (Odaka et al., 2003).

In the cases where a network of stations is deployed in the source area, network-based EEW systems analyze the early P-wave signals recorded at the stations, detect the occurrence of the earthquake, determine its location and magnitude and estimate its shaking potential to nearby and distant sites, using previously calibrated empirical attenuation relationships (Ground Motion Prediction Equations, GMPE). The alert notification can reach any distant site within a time interval from the earthquake origin that typically ranges from a few seconds (few tens of kilometers from the source) to several tens of seconds (a hundred kilometers from the source). Different factors may influence the “lead-time”, i.e., the delay between the arrival of the strongest shaking waves at the target site and the first alert time. Among them, the distance between the source area and the target site, the geometry of the network, the time of event detection, the time needed for the automatic waveform analysis and telemetry and, lastly, the complexity of the source.

During the last two decades EEW systems have been widely developed and experimented in several high seismic hazard countries around the world, such as Japan, USA, Mexico, Taiwan, and China (Allen and Melgar [2019]). In Europe, several active seismic countries, mostly along the Mediterranean region (Italy, Romania, Switzerland, Turkey, Greece, and the Ibero-Maghrebian region), are nowadays experimenting and testing the use of EEW systems mainly for research purposes, while the technological components of the operational seismic monitoring systems are yet not fully real-time compliant, such that they can be an effective tool for fast seismic risk mitigation actions (Clinton et al. [2016]).

Most of the existing EEW systems are based on the standard concepts either of the network-based system or of the on-site approach. In some cases, such as in Japan, where the station density and

coverage are high and uniform all over the country and where the largest magnitude earthquakes may occur offshore, the nation-wide EEW systems benefit from the early P-wave detection at coastline stations (in an on-site approach), for issuing the warning at inland sites. However, the actual integration of the onsite and network-based approaches is under development in Japan, USA and China for providing the output for a timely and robust alert decision scheme.

The Japan Meteorological Agency (JMA) is currently testing the propagation of local undamped motion (PLUM) method (*Kodera et al. [2018]*), a wavefield-based EEW approach that predicts seismic intensities directly from spatial inter- and extra-polation of the observed real-time ground motion measures near target sites. When integrated with standard point-source EEW methods, the PLUM method showed an improved performance in terms of more accurate ground-motion prediction for large earthquake rupture and event detection and declaration in case of multiple events sequences.

Whichever configuration is used, the standard approaches to EEW are based on simplified assumptions and models both for the earthquake source and wave propagation processes. This may result in highly uncertain predictions of the earthquake peak shaking and therefore in an unacceptable large number of missed or false alarms (*Minson et al. [2019]*).

To account for the earthquake source finiteness, different methodologies have been recently proposed and developed to estimate in real-time the fault geometry and size from early P and S-wave signals collected at near-source stations.

The FinDer (Finite Fault Rupture Detector) algorithm (*Böse et al. [2012]*), assumes a line source and can automatically detect in real-time its surface projection, the current centroid position, length, and strike, by comparing the real-time ground motion amplitudes to a set of pre-calculated templates, using image recognition techniques. Errors in length estimates are typically on the same order as station spacing in the network so that the method turns out to be useful for accurate earthquake early warnings wherever the station density is sufficiently high.

Real-time inversion of amplitudes recorded by high-frequency GPS stations have also been explored to improve the finite fault description in terms of magnitude and source length (*Allen and Ziv [2011]; Colombelli et al. [2013]; Grapenthin et al. [2014]*). In these approaches, the permanent static offset produced by large earthquakes (i.e., the coseismic ground deformation) is inverted in real-time to infer the slip distribution on the fault plane, assuming a prior determined fault orientation. The real-time magnitude and the along-strike extent of the rupture area are finally used to predict the expected ground shaking due to the finite source.

More recently, the progressive measurement of the P wave displacement amplitude has been proposed to obtain a fast characterization of the extended earthquake source, in terms of magnitude and expected length of the rupture (*Colombelli and Zollo [2015]; Nazeri et al. [2019]; Zollo et al. [2021a]*). In this approach, the Logarithm of P-wave amplitude vs Time (LPDT curve) is used as a proxy for the Moment Rate Function, allowing for the real-time tracking of the source process evolution and for a rapid characterization of seismic moment and source rupture duration, in the hypothesis of a triangular shape for describing the source process.

Here we present a new methodology that integrates the network and on-site approaches for the alert release. The methodology is based on the real-time, evolutionary mapping of the Potential Damage (or strong shaking) Zone (PDZ) as represented by a predicted Intensity Measure (IM), such as the peak ground velocity/acceleration or the instrumental intensity. The methodology incorporates the more recent techniques for a refined estimation of the main source parameters (earthquake location and magnitude) and P-wave-based, peak motion forecast (e.g., *Colombelli and Zollo, 2015; Caruso et al., 2017 and Zollo et al., 2021*) that are used to predict the expected ground shaking level at sites not instrumented by strong motion sensors.

Previous studies, in several seismic regions worldwide, have shown that the P-peak initial amplitude is a natural proxy for the late maximum amplitude of seismic records acquired from near-source to regional distance range (epicentral distance < 100 km) (*Wu and Kanamori [2005];*

Zollo et al. [2010]). An empirical log-log relationship is usually adopted to correlate the Peak ground motion on the entire signal (in acceleration - PGA - or velocity - PGV) to the initial P-wave peak amplitude ( $P_a$ ,  $P_v$  or  $P_d$ ), measured in a short time window (1 to 5 s) after the P-wave arrival. These empirical relations have been proposed and used in onsite EEW applications to predict the peak ground shaking of the potential damaging event, by-passing the estimation of source magnitude and location.

In the proposed method, previous calibrated empirical relations between early P-wave amplitudes and peak ground motion parameters are used to predict the shaking intensities at instrumented, recording sites. As the P wavefront propagates across the network, a time-varying, *early* shake map is built through a physics-based interpolation approach, which combines the available observed, P-wave and GMPE predicted PGV (following Worden et al. [2010]).

Here we evaluate the performance of the proposed methodology through its offline application to the October 30, 2016,  $M_w$ 6.5 Norcia (Central Italy) earthquake records and discuss the system performance in forecasting the earthquake peak ground shaking.

## **2. METHOD**

The methodology combines specific modules aimed at sequential operations, going from earthquake detection and location to magnitude determination and peak ground shaking prediction. The block diagram of the method is shown in Figure 1, while the detailed theory and implementation of the main steps are described separately in the following sections. The adopted strategy is to combine the principles of onsite EEW methods (Peak ground shaking prediction by P-wave amplitude measurements) and those of network-based approaches (real-time location, magnitude estimation and PGV prediction through regional-specific GMPEs).

### **2.1 Earthquake detection and location**

The system is designed to process the 3-component, ground acceleration records, as acquired by a real-time, dense network deployed in the earthquake epicentral area and extending to local and regional (100 km) distances. The first P-wave arrival time signals are detected by the real-time Filter-Picker 5 algorithm (*Lomax et al. [2012]*) on the vertical component of the acceleration waveforms.

As soon as the first two stations have triggered the event, a real-time location estimate is obtained by using a real-time version of the M-PLOC algorithm described in *Zollo et al. [2021b]*. M-PLOC provides a probabilistic solution for the earthquake location, based on the real-time measure of three different observed quantities (differential arrival times, amplitude ratios, and back-azimuth from the P-wave polarization) evaluated in progressive (or fixed) time windows after the first P-wave arrival. The most probable estimates of hypocenter coordinates and origin time are provided as soon as the first stations trigger the event and are progressively updated as the P-wave front expands across the network and new portions of signals are acquired by more and more distant stations. In the present application only the differential arrival times at pairs of stations within the network have been used for earthquake location, since preliminary tests confirmed that the azimuthal coverage of stations was sufficiently dense to get optimal location without using additional parameters.

When using only differential P-arrival times, the M-PLOC method determines the earthquake location as the maximum likelihood location contained in a gridded 3-D crustal volume. A minimum of 2 stations where the first P-arrival is detected are used to get the first earthquake location. In this case the epicenter location is set at the half-length of the surface segment joining the two station locations and a trial-depth value is assumed. In the the case-study application considered in this paper a trial-depth of 10 km has been set based on the historical seismicity of the area, but this initial value can be adjusted according to the characteristic depth distribution of historical seismicity in other seismic regions of interest. However, after few iterations this initial

location is updated as more P-wave arrival time data are available. With three or more stations at which the P-arrival is detected, the mutual differential times allow to constrain the hypocenter location with an accuracy that is progressively improved as more P-arrival times are available from the automatic picking. Details about the earthquake location uncertainty estimates inferred from the PDF distribution can be found in Zollo et al. [2021b].

## 2.2 Peak parameter measurement

Following the onsite method and starting from the P-wave arrival time, we measure the initial peak amplitude parameters,  $P_a$ ,  $P_v$  and  $P_d$ , as the absolute, maximum value of the vertical component of acceleration, velocity and displacement, respectively. The measures are repeated every 0.5 sec and are stopped at the expected arrival of the S-waves, as predicted by the earthquake location. The acceleration records are first processed by removing the mean value and the linear trend. Waveforms are then integrated once to obtain velocity waveforms and the linear trend is removed again, prior to measure  $P_v$ . A second integration is performed to get displacement traces, followed by a causal, high-pass Butterworth filter, to remove the artificial low-frequency drifts and baselines on displacement traces, which may appear from the double integration operation (Boore et al. [2002]). Following the approach already used by Caruso et al. [2017], we automatically select the proper cut-off frequency for the filter, which can be either 0.075Hz or 1Hz, depending on the quality of the input data, as briefly recalled in the following lines. Two parameters are used to evaluate the quality of data: the signal-to-noise ratio ( $SNR$ ) and the  $P_d/P_v$  ratio. Specifically, the  $SNR$  is computed as  $SNR = 20 * \log_{10}(P_d/P_d^N)$ , where  $P_d$  is measured on the available signal in the selected time window and  $P_d^N$  is the maximum displacement of the pre-event noise, over the same time window. As for the  $P_d/P_v$  ratio, both peak amplitude parameters are measured in the same time window. Based on the idea that  $P_d$  and  $P_v$  follow a linear, constant-coefficient empirical relation with magnitude and logarithm of



hypocentral distance, their ratio is therefore expected to vary in a predetermined range around a constant level. On the contrary, out-of-range  $P_d/P_v$  values indicate noisy data, with the peak displacement possibly contaminated by artificial long-period distortions. The observed values of  $SNR$  and of the  $P_d/P_v$  ratio are therefore compared to predetermined threshold values, for the automatic selection of the proper filter, or data are eventually discarded if the quality control is failed (see *Caruso et al.* [2017], for further details).

### 2.3 Magnitude estimation

As in network-based approaches, in our method the real-time moment magnitude ( $M_w$ ) is obtained by averaging the single magnitude estimates derived from the three P-peak amplitude parameters ( $P_a, P_v$  and  $P_d$ ), measured at few near-source stations. Given a recording station at hypocentral distance  $R$ , for each parameter, we use an empirical attenuation relationship to estimate the moment magnitude, of the form (*Wu et al.* [2006]; *Zollo et al.* [2006]):

$$M_w^x = A_x \cdot \log P_x + B_x \cdot \log R + C_x \quad \#(1)$$

where  $x = a, v, d$  indicates acceleration, velocity and displacement P-waveform records. The method requires that the coefficients of eq.(1) should be previously derived from the retrospective, empirical regression analysis of different magnitude-distance earthquake records in the seismic region of concern. In this study, for demonstration purposes, the coefficients  $A_x, B_x$  and  $C_x$  are determined by a linear regression analysis using an existing earthquake data set in Central Italy, the region of our earthquake-application case study (see section 3)

For a given station  $i$  and for each time step  $t$ , the magnitude value is obtained by the weighted average of all the available predictions:

$$M_w^{it} = \frac{w_a \cdot M_w^a + w_v \cdot M_w^v + w_d \cdot M_w^d}{w_a + w_v + w_d} \quad \#(2)$$

where the weights  $w_x$  are estimated from the standard errors  $\sigma'_x$  of empirical relations (1) as

221  $w_x = \frac{1}{\sigma_x'^2}$ . Finally, considering that at the time step  $t$ , a total of  $N$  stations has recorded the P-wave  
222 signal with a variable signal length  $T_d^{it}$  ( $i$  is the station index), the final, average magnitude is  
223 obtained as:

$$M_w^t = \frac{1}{\sum_{i=1}^N T_d^{it}} \sum_{i=1}^N T_d^{it} \cdot M_w^{it} \quad \#(3)$$

224 where the signal length  $T_d^{it}$  is used to weigh the station-magnitude values. Here we assume that  
225 the estimates inferred from larger portion of P-wave signals must have a larger weight than those  
226 obtained from shorter time windows. In our approach, the magnitude is computed using only  
227 stations that satisfy a specific criterion, as explained below.

228 A previous study (e.g., *Colombelli et al. [2015]*) has shown that the joint use of the three P-peak  
229 amplitude parameters allows improving the accuracy and reducing the uncertainty on magnitude  
230 estimation, especially when a limited time window and number of stations are available for the  
231 measurement. Furthermore, initial P-wave observation of real earthquakes have shown that when  
232 expanding the time window, the three peak amplitude parameters generally increase with time.  
233 The typical Logarithm of P-peak Displacement vs Time (LPDT) curve starts from small values and  
234 reaches a stable plateau level at a corner-time that depends on the final event magnitude  
235 (*Colombelli et al. [2012; 2014]*; *Trugman et al. [2019]*). Additionally, *Colombelli and Zollo [2015]*  
236 observed the dependency on magnitude of this corner-time and used it to estimate the fault  
237 length of earthquakes in Japan. *Nazeri et al. [2019]* and *Trugman et al. [2019]* confirmed this  
238 general behavior of LPDT curves by analyzing extended datasets for Japanese and Central Italy  
239 earthquake sequences. More recently, *Zollo et al. [2021a]* propose a technique to determine the  
240 rupture radius of a circular earthquake rupture from the estimations of the corner-time of  
241 azimuthally averaged LPDT curves.

242 Given the general increasing amplitude of initial P-wave peak parameters with time, reliable  
243 magnitude estimates can be obtained only for  $P_x$  values measured at the plateau of the curves,

while significant magnitude underestimations can generally occur using shorter time windows (i.e., while the curve is still increasing). In our method, to avoid the initial underestimations, we developed an automatic algorithm able to identify the plateau time of the curves, by continuously monitoring their time derivative and evaluating when it reaches a near-to-zero threshold value. At this time, i.e., when the plateau has been reached, the corresponding peak parameters start being used for the magnitude determination. It is worth to note that the three curves (LPAT, LPVT, and LPDT) are expected to reach the plateau level nearly at the same time (Colombelli *et al.* [2014]; Nazeri *et al.* [2019]), thus, for computational simplicity, we only monitor the time derivative of the LPVT curve. Figure 2 shows some examples of recorded seismograms (in acceleration) at a few stations around the epicenter and the corresponding computation of LPDT curves, which are available at sequential times, as the P-wave front propagates across the array. Finally, to ensure a rapid convergence to the final magnitude of the event, only the recordings within 100km from the epicenter are used for the magnitude computation, or alternatively a maximum of 30 triggered stations.

#### 2.4 Computation of the “Early” Shake-Map

With the aim of building real-time reliable, P-wave based, shake maps, we predict the peak ground motion in the region of interest using two different approaches, one for the recording sites and another for the *virtual* nodes, i.e., the not-instrumented grid nodes. Specifically, the Peak Ground Velocity (PGV) at the recording sites is predicted from the recorded P-amplitudes of the early P-wave signals using eq. 1 (onsite approach). The PGV at the *virtual* nodes is instead predicted through a physics-based interpolation techniques which uses the available regional ground motion prediction equation (GMPE) and real-time estimates of earthquake location and magnitude (network-based approach). The two approaches are described in detail in the following sections.

##### 2.4.1 Peak ground motion prediction at the recording sites

Like what has been done for the magnitude, the three peak amplitude parameters  $P_a$ ,  $P_v$  and  $P_d$  measured at the recording sites for each time window  $t$ , are jointly used to predict the expected PGV, based on a scaling relationship of the form:

$$\log PGV_x^t = D_x \cdot \log P_x^t + E_x; \quad w_x = \frac{1}{\sigma_x^2} \quad (4)$$

Where  $D_x, E_x$  are the empirically estimated coefficients and  $\sigma_x$  are the standard errors of the relationship between the  $PGV$  and the  $P_x$  parameter. Coefficients  $D$  and  $E$  are empirically estimated using a linear regression analysis, for each peak amplitude parameter ( $P_x$ ) and each time window ( $t$ ). An example of data and linear regression for the 3-s time window is shown in Figure S3 of the Supplemental Material, while the full list of estimated coefficients (and their uncertainties) is reported in Table S2 of the Supplemental Material. The predicted value of  $\log PGV$  and its uncertainty at any time  $t$  are therefore obtained as the weighted average of the three estimated  $\log PGV_x^t$  values:

$$\log PGV_{onsite}^t = \frac{w_a \cdot \log PGV_a^t + w_v \cdot \log PGV_v^t + w_d \cdot \log PGV_d^t}{w_a + w_v + w_d} \quad \#(5)$$

$$\sigma_{\log PGV_{onsite}} = \sqrt{\frac{w_a \cdot \left(\log \frac{PGV_a^t}{PGV_{onsite}^t}\right)^2 + w_v \cdot \left(\log \frac{PGV_v^t}{PGV_{onsite}^t}\right)^2 + w_d \cdot \left(\log \frac{PGV_d^t}{PGV_{onsite}^t}\right)^2}{w_a + w_v + w_d}} \quad \#(6)$$

Coefficients  $D$  and  $E$  of equation (4) are region-specific and must be preliminary determined through analyses that use data from past earthquakes recorded in the region of interest. Furthermore, the algorithm is designed to monitor both the vertical and the horizontal components. The predicted PGV from the vertical  $P_x$  amplitude is continuously compared to the PGV value measured on the horizontal components. At any time along the waveform, the maximum between these two values is used as the peak ground motion estimate.

At the end of the event (set at fixed time window of 30 seconds after the first P-wave arrival in our

application) for each seismogram, the final PGV measured as the maximum of the North-South and East-West horizontal components, replaces the last P-wave predicted one, so that the evolutive, “early” P-based, PGV predictions naturally converge toward the final PGV values.

#### 2.4.2 Peak ground motion prediction at “virtual” nodes

At each time step  $t$ , the prediction of PGV at the not-instrumented sites of the grid map, is obtained using a physics-based, interpolation algorithm combining the available information from recording stations and the regional scale predictions. Specifically, with the same approach as used for the shake-map computation (Worden et al. [2010]), the PGV at the time  $t$  is obtained through the following relationships:

$$PGV^t(x, y) = \frac{\sum_{i=1}^N \left[ \frac{1}{\sigma_{i2}^2} \cdot PGV_{onsite}^t \right] + \frac{1}{\sigma_{GMPE}^2} \cdot PGV_{GMPE}(x, y)}{\sum_{i=1}^N \left[ \frac{1}{\sigma_{i2}^2} \right] + \frac{1}{\sigma_{GMPE}^2}} \quad \text{for all station } i \text{ with } r_{\Delta} > 0 \quad (7)$$

where:

$PGV_{onsite}$ : the PGV predicted at network stations from P-peak amplitudes through equations (5) and (6);

$PGV_{GMPE}$ : the PGV predicted by a regional GMPE given the available estimates of earthquake location and magnitude. In our applications we used the GMPEs derived by Bindi et al.[2011] for Italy.

$$\sigma_{onsite}^i = \sigma_{PGV} \cdot (1 - \exp(-\sqrt{0.6 \cdot r_{\Delta}})) \quad \text{for } r_{\Delta} \leq R_{roi}$$

$$\sigma_{onsite}^i = (\sigma_{onsite}^i | r_{\Delta} = R_{roi}) \cdot \frac{r_{max} - R_{roi}}{r_{max} - r_{\Delta}} \quad \text{for } r_{max} \geq r_{\Delta} > R_{roi} \quad (8)$$

$$\sigma_{onsite}^i = \infty \quad r_{\Delta} \geq r_{max}$$

with:

- 313 -  $PGV^t(x, y)$ , the PGV predicted at the virtual node located at  $(x, y)$ ;
- 314 -  $r_{\Delta}$ , the distance between the  $i$ -th network node and the virtual node;
- 315 -  $\sigma_{GMPE}$ , the standard error of the used GMPE;
- 316 -  $\sigma_{PGV}$ , the standard error of the P-wave predicted PGV retrieved from equation 6;
- 317 -  $R_{roi}$  ( $roi$ =region of influence), the distance of the area around the network stations where the
- 318 observed data influence the PGV interpolation more than the PGV estimate through the GMPE
- 319 ( $PGV_{GMPE}$ );
- 320 -  $r_{max}$ , the limiting distance of the area where the observed data influence the interpolation.
- 321

322 Like their implementation in the ®Shakemap algorithm (Wald et al., 2006), the parameters  $R_{roi}$

323 and  $r_{max}$  are user configurable, depending on the network aperture and inter-station distance. The

324 errors in earthquake location and magnitude on PGV predictions, which are variable and sharply

325 decreasing with time, are not explicitly considered in the present formulation but generally

326 accounted by the standard errors on GMPE and on the PGV vs P-amplitude relations. Previous tests

327 of location and magnitude determination (see Zollo et al., 2021b) using earthquakes with different

328 magnitudes and locations show that in cases of relatively high dense networks around the

329 epicenter, the errors on magnitude and location using real-time methods after only few seconds

330 become comparable to ones obtained offline and using all the network stations and the effect on

331 the predicted PGV (by GMPE) is similar to what is expected in the shakemap computation. After

332 several trials, in our application to the central Italy network we used a value of  $R_{roi} = 15 \text{ km}$  and

333  $r_{max} = 30 \text{ km}$ . The interpolation formula of equation (7) is valid for all points  $(x, y)$  at the surface,

334 except for those where stations are located, where the predicted PGV is obtained from equation 5.

335 Starting from the first P-wave arrival time, equations (7) and (8) allow predicting the PGV and its

336 uncertainty at any point of the area surrounding the epicenter. This PGV value is expected to vary

337 with time as new data become available from stations located at increasing distances from the

epicenter and to finally stabilize at a constant value for a high number of station amplitude data and wide P-wave time windows. We note that the maximum P-window length is chosen according to the expected S-arrival time, which is the same criterion used to determine the empirical relations (4).

The final output is the predicted PGV vs. time at any position (x,y) around the earthquake source, which can be finally converted to instrumental intensity through regional empirical relations (e.g. *Faenza and Michelini* [2010], for Italy) to be included in the early warning alert broadcast message.

### **3. Application to the Mw 6.5, October 30, 2016 Norcia (Central Italy) earthquake**

We performed an off-line application, by simulating the real-time data streaming of the 2016 October, 30, Mw 6.5 Norcia (Central Italy) earthquake (Figure 2). The event was caused by the activation of an about 20 km long system of two normal faults along the Central Apennine chain, rupturing two main slip patches (peak-slip  $\sim 3$  m) and producing a strong ground shaking and severe building damage and collapses in a wide area extending over 50 km distance around the epicenter (*Scognamiglio et al.* [2018]). According to *Scognamiglio et al.* [2018] the rupture nucleated at about 9 km depth and propagated up-dip and south-eastward along the N155°E fault with a rupture velocity of 2.8 km/sec and then triggered a secondary rupture on a smaller fault, 10 km southern of the main fault epicenter, with a clockwise rotated strike direction (N210°E). The two rupture episodes produced average fault slips of 0.4 and 0.6 meters with seismic moments  $5.9 \times 10^{18}$  Nm and  $2.9 \times 10^{18}$  Nm, respectively. The maps of strong ground shaking (expressed in MCS intensity scale, Peak Ground Velocity and Peak Ground Acceleration) are reported in the November 2016 INGV Working Group' report (*Gruppo di Lavoro INGV*, [2016]). The maps are computed using the peak ground shaking data available from the European Strong Motion database (*Luzi et al.* [2016]) containing the earthquake waveforms from a total set of 240 stations with a maximum epicentral distance of 673 km. The shaking intensity reported in the map ranges

from IV to IX, with the level of VI, corresponding to “strong perceived shaking” in the MCS scale (PGA of 4.8 %g and PGV 2.4 cm/sec), affecting a wide portion of the Central-Italy territory and extending over an area of about 100 km radius out of the epicenter.

For our simulation, we used the three component earthquake records acquired by 60 stations of the Italian Accelerometric Network (RAN) located within an area of 50 km radius centered at the event epicenter (Figure 2). The selected sub-network provides a rather dense azimuthal and distance coverage of the source with an average inter-station spacing of 15-20 km.

The coefficients of eq. 1 have been preliminarily determined by a linear regression analysis using an existing earthquake data set spanning a wide magnitude ( $M_w$  3.5 – 6.5) and distance ranges ( $R$  0-100 km). The dataset for calibrating the coefficients of eq.1 did not include the waveforms of the analysed  $M$  6.5 earthquake in the Norcia region. We used a total number of 286 earthquakes and 3786 records (3 components each) from 504 RAN and INGV stations. The data have been gathered from the ITACA database - <http://itaca.mi.ingv.it> (Luzi et al. [2019]). Details about the calibration dataset are reported in Text S1 of the Supplemental Material. The empirical regression coefficients (A, B, C) and their uncertainties are reported in Table S1 of the Supplemental Material, together with the standard error of the regression. Plots of calibration data and scaling relationships are shown in Figure S2 of the Supplemental Material.

Figure 3 shows the time changes of the location error (distance in km from the INGV bulletin solution) and moment magnitude, using the P-wave arrival times and peak amplitudes available at each time step, as the P-wave front progressively expands across the network. In the EEW method these data are used to update the PGV predictions at virtual nodes (eq.7) using the specific GMPE for Central Italy. The moment magnitude estimated by the EEW method is generally smaller (first estimate,  $M_w$  5.6, late estimate  $M_w$  6.2) relative to offline measures using regional and teleseismic S and surface waves (6.5+) while it is better consistent with  $M_{wp}$  (6.3) but still underestimated. In this case, the difference of -0.1 between the EEW- $M_w$  and  $M_{wp}$  can be attributed to the shallower



hypocentral depth (about 6 km, relative to the bulletin depth of 9 km) determined in RT by the EEW method using only near-source P-wave arrival-times. We note that despite the underestimation of the final earthquake depth and moment magnitude, as discussed later in this article, the EEW method can predict and track with great accuracy the peak ground shaking area, this information being used for early warning.

Figure 4 shows the space-time evolution of the P-wave-based prediction of instrumental intensity ( $I_{MM}$ ) (derived from PGV through the empirical relations of *Faenza and Michelini* [2010]). Snapshots are shown at different times from the event origin time.

The Potential Damage Zone (PDZ) is here defined as the area where the predicted peak ground velocity is larger than a threshold. In our method this is quantified in terms of instrumental intensity ( $I_{MM}$ ) (derived from PGV through the empirical relations of *Faenza and Michelini* [2010]) with a threshold ( $I_{MM}=VII$ ) that, in the "shakemap" implementation in Italy by INGV, is associated with the potential impact level of "very strong shaking" and "moderate" damage. The chosen PGV threshold corresponds to the minimum intensity for which damage of buildings can potentially occur in Italy, according to the reference Intensity vs PGV relationship of *Faenza and Michelini* (2010). A different intensity scale or ground motion intensity measure can be adopted and easily implemented in the approach when exporting the methodology to other areas than Italy.

The PDZ is observed to clearly expand with time, changing its shape and extent, as new data from the P waves propagating across the array are available. At its initial stage (4-5 sec, Figure 4a,b) the PDZ assumes a near-circular shape, since it is totally controlled by the GMPE-predicted PGV, with the contribution of only few near-source stations. At larger times (10-30 sec, Figure 4c,d,e) the PDZ depicts a nearly elliptical area with a predominant elongation to south-east of the epicenter. The anisotropic shape of the PDZ is the effect of larger P-wave and PGV-predicted amplitudes toward the South-East direction which is consistent with a dominant SE earthquake rupture propagation,

as revealed by the kinematic source modelling of near-source strong motion and GPS records (Cheloni et al. [2017]).

A precautionary first alert could be issued to the whole region of interest at the time of the first alert (around 4 sec) when a ground shaking of  $I_{MM} \geq VII$  is predicted to affect a wide near-circular area (radius 30 km) around the epicenter.

After about 15-20 seconds from the first P-arrival at the network, the shape of the PDZ remains stable and unchanged even adding the contribution of more distant stations (Figure 3d,e). A qualitative comparison of the 15 sec “early” shake-map (Figure 3d) with the final released by INGV (Figure 4f) shows a very good matching of  $I_{MM} > VII$  areas between P-wave predicted and final ground shaking maps. In particular, the rupture directivity toward SE is evident from the shape of the PDZ dominantly elongated in this direction.

We define the “time of the first alert” ( $T_{FA}$ ) as the time measured from the origin time (OT), at which the first PGV (IMM) prediction overcomes the threshold for the alert, that has been set to PGV=3.9-4 cm/sec for IMM=VII, following the scale proposed by Faenza and Michelini [2010]. In our simulated scenario,  $T_{FA}$ =3.6 sec, which accounts for the P-wave propagation from the earthquake depth to the surface and for the time required to get to the plateau level of LPDT curves at the two stations nearest to the epicenter.

The early warning system performance for this single earthquake scenario can be assessed as the ability of the system to forecast the earthquake shaking and potential impact (IMM, instrumental intensity above the threshold) in terms of the number of successful (positive and negative), missed and false alerts.

In detail, we can define the following criteria:

**Successful Alert (SA):** 
$$I_{MM}^{pred} \geq I_{MM}^{thre} \text{ \& } I_{MM}^{obs} \geq I_{MM}^{thre} \quad (9a)$$

**Successful No-Alert (SNA):** 
$$I_{MM}^{pred} < I_{MM}^{thre} \text{ \& } I_{MM}^{obs} < I_{MM}^{thre} \quad (9b)$$

**Missed Alert (MA):** 
$$I_{MM}^{pred} < I_{MM}^{thre} \text{ \& } I_{MM}^{obs} \geq I_{MM}^{thre} \quad (9c)$$

438 **False Alert (FA):** 
$$I_{MM}^{pred} \geq I_{MM}^{thre} \text{ \& } I_{MM}^{obs} < I_{MM}^{thre} \quad (9d)$$

439 where  $I_{MM}^{thre} = VII$

440 We evaluate the performance of the EEW method at times  $T_{FA}=3.65\text{sec}$ ,  $T_{FA} + 0.5 \text{ sec}$  (4.15 sec)  
441 and  $T_{FA} + 1.5 \text{ sec}$  (5.15 sec), all times evaluated since OT (Figure 5). Indeed, we expect that the  
442 performance of the system should improve as a function of the time, since additional recorded P-  
443 amplitudes become available and more accurate estimations of the earthquake location and  
444 magnitude are derived from distant stations.

445 Figures 5a,b and c show the performance of the system at the three different times in terms of SA  
446 (dark green), SNA (light green), MA (red) and FA (yellow) with colored circles at the station  
447 locations.

448 At 3.65 sec after OT (Figure 5a), the percentage of successful alerts (SA+SNA: 57%) is slightly higher  
449 than missed/false alerts (MA+FA: 43%) considering the whole area covered by the seismic  
450 network, while it reaches near 71% when considering epicentral distances smaller than 40 km.  
451 Indeed, at this time, the majority of missed alerts are issued at the largest distances from the  
452 epicenter ( $R > 30\text{-}40 \text{ km}$ ).

453 Half a second later (Figure 5b), the shaking forecast performance highly improves, with an overall  
454 increase of the percentage of successful alerts (both SA and SNA), reaching 92%, when considering  
455 the whole 55 km radius area. At this time, a single SNA and MA are recorded, with 4 FA (6.6%).  
456 Within a circle of 40 km epicentral radius we measure 98% of SA with just one FA at a station not  
457 far from the circle. At  $T_{FA}+1.5\text{sec}$  the system performance evolves to a condition where only SA  
458 (92%) and FA (8%) are recorded. All FAs except one are recorded at outside the 40 km radius,  
459 where all sites still record all SAs except a single FAs.

460 The change with time of the relative proportion of SA, SNA,FA and MA is a typical effect of our  
461 evolutive early warning systems that will be discussed later in the paragraph “Discussion”.

462 Concerning the lead-times, these are estimated as  $T_{LT} = T_S - T_{FA}$ , where  $T_S$  is the predicted S-

463 wave arrival time given the earthquake location and the average crustal velocity values ( $V_p=5.5$   
464 km/s;  $V_s=3$  km/sec) for the area. Although a more complex calculation of the lead-time using the  
465 observed S-wave arrival time could have been implemented, here we meant to provide an  
466 approximate estimate of the lead-time as a function of the distance, having preliminary verified  
467 that the observed S-wave arrival is within  $\pm 0.3$  seconds than what predicted by a homogeneous  
468 crustal velocity model.

469 The map of lead-times (Figure 6) shows values ranging from 2 s to 14.6 sec at 15 km and 55 km  
470 from the epicenter, respectively. For the considered event and station distribution the *blind-zone*,  
471 e.g., the area where the first S-waves are expected to arrive before the alert is issued, covers a  
472 circular surface with a radius of 6.5 km centered at the epicentral position.

#### 474 **Discussion**

475 We propose a new earthquake early warning method where the alert is issued based on the  
476 progressive tracking of the potential damage zone (depending on the chosen PGV/IMM threshold)  
477 which is mapped using a predicted PGV value resulting from the physics-based interpolation of the  
478 recorded P-amplitude and GMPE-derived PGV values. The GMPE values are determined using the  
479 earthquake location and magnitude estimated by near source recording of early P-wave signals. An  
480 update of PGV/IMM predictions is done as new locations and P-wave data are available from more  
481 distant stations. Since it is based on the recorded ground motion P-amplitudes at stations around  
482 the epicenter, the proposed technique naturally accounts for the spatial variability of strong  
483 ground motion related source (i.e., rupture directivity), crustal wave propagation and site  
484 amplification as inferred from the early P-signals.

485 The onsite PGV at instrumented sites is predicted from the P-peak acceleration, velocity and  
486 displacement values measured on the original vertical component record. In this study, the  
487 empirical relations  $\log \text{PGV}$  vs  $\log (P_d, P_v, P_a)$  have been determined and calibrated for the Central

Italy region using the available waveform data-bank for previous earthquakes in the magnitude range 3-6.5 and distance interval 10-100 km.

The use of the three P-amplitude, observed parameters showed to improve, in general, the accuracy of the predicted PGV relative to the use of a single parameter, since they carry on information about the P-amplitude in different frequency bands. In addition, since the P-peak amplitude for moderate-large earthquakes is expected to increase with time from the first P-arrival, the method implements an algorithm allowing to start measuring the P-amplitude only after the LPDT curves reach their plateau. This would make more robust the technique by reducing the number of missed alerts at the expenses of a longer P-wave time window to explore. Recently *Colombelli et al.* [2014, 2020] showed that the initial slope of the LPDT curves scales inversely with the earthquake magnitude, suggesting that this initial slope parameter could be used as a proxy for the rapid assessment of the earthquake size during an ongoing rupture. Future developments of the described method will include initial slope measurements to provide constraints on the ongoing event magnitude, to be used for a faster time of the first alert.

The proposed methodology integrates the principles of onsite EEW methods with those used for network-based approaches, to provide reliable and physics-based estimations of the expected shaking distribution. An intrinsic advantage of the methodology is the capacity of being adapted to a variety of potential stakeholders and target applications, that could make use of outcomes of the method in different ways. For example, on-site estimates could be used to control dedicated actions at specific sites (such as industrial settlements, schools, hospitals), while distributed targets (as the case of railway applications) could benefit from the real-time regional mapping of the expected shaking to trigger automatic emergency measures as slowing-down/arrest high-speed trains, disrupting the gas/electric energy supply to a pipeline, halting the high-way circulation of vehicles transporting hazardous materials.

The off-line application of the EEW method to the M 6.5 October,30, 2016 Norcia earthquake in

Central Italy shows the reliability and robustness of the methodology. It provides a rapid alert message with a time-varying assessment of the earthquake shaking and potential impact as obtained by the algorithm of data interpolation able to build a realistic, P-wave-based, “early” shake map. We showed that the latter is very consistent with the shake-map computed by INGV tens of minutes after the earthquake occurrence, using the recorded PGV data on the horizontal components at strong motion stations over a wide distance range.

The considered scenario case confirms a good performance of the system in terms of reliability of the predicted intensity map which naturally includes the spatially variable ground motion shaking as originated by source directivity effects, although inferred from near-source recorded P-amplitudes. This is already visible on maps after few seconds from the first P-wave recorded at the near-epicenter stations.

The rapidity of the system in processing data and releasing the warning along with the reliability of ground shaking predictions may depend on the network density and azimuthal coverage in the epicentral area. However, the joint use of regional-scale and on-site predictions for the ground shaking distribution is expected to provide better constrained predictions, even in those situations where the distribution and coverage of stations are non-optimal. This could be the case, for example, of off-shore subduction earthquakes (such as the 2011, Tohoku-Oki earthquake), for which we expect that the addition of coastal stations will strongly constrain the regional-predicted shaking distribution, as discussed by Colombelli et al., (2012) when rapidly mapping the Potential Damage Zone for this event.

We showed that the capability of the EEW system to predict the strong motion above the threshold improves with time. Only 1.5 sec after the TFA (5.15 sec after the OT) the performance of the system in predicting the event peak shaking is very high: in the area of 40 km radius around the epicenter, that impacted an Intensity MCS VIII-IX as estimated by INGV shakemap), all 42 instrumented sites except one showed a successful alert with only one false alarm. Considering the

calculated blind-zone of 6.5 km radius, there is still a wide annular area, where the alert could have reached the population before the strong ground shaking occurrence.

In Figure 5c, the circular blind-zone and lead-times are calculated at  $T_{FA}=3.65$  sec which corresponds to the time of the P-waves detected at the first two stations, and when the first location, magnitude estimations and peak amplitudes are available. According to this simulation, only 1 municipality of the 170 located within 55 km of the epicenter and belonging to the regions of Abruzzo, Marche, Umbria and Lazio, would be located within the blind-zone. For these 2 municipalities the minimum negative lead-time is -0.5 sec at the town of Norcia, i.e. half-second is the maximum time in advance of the S-wave arriving at these sites before the alert issuing.

Even considering a later first alert, i.e., at 5.15 sec after the OT, the calculated blind-zone radius would have been 15 km long. 165 municipalities, located in the 15-55 km circular ring around the epicenter show positive lead-times, and might have been alerted 2 to 14.5 sec in advance to the arrival of the first S-wave at those sites.

At  $T_{FA}=3.65$  sec, for 26 of the 60 accelerometric station sites, located at epicentral distances between 25 and 55 km, the EEW system incorrectly predicts a PGV below the threshold (e.g. a missed alert, MA). The numbers of MA at  $T_{FA}=3.65$  sec for distant sites is mainly due to the underestimated PGV predicted by the GMPE with an initial lower magnitude as evaluated from near-source stations while using short P-wave time windows. As the time increases, larger portions of the P-wave time window are considered for the analysis and sites previously labelled as MA or SNA evolve towards SA and FA, respectively, with a final picture where only successful and false alerts are declared at the network. This is a common characteristic of similar time-evolutive EEW system that naturally tend with time to increase SA and FA at the expenses of MA and SNA.

This effect can be explained starting from the definitions of SA, SNA, MA and FA, provided by equations 9a,d. For each of the four possible situations, indeed, the second member of inequalities (related to  $I_{MM}^{obs}$ ) does not change with time at the recording nodes. The first condition (related to

the predicted intensity ( $I_{MM}^{pred}$ ), instead, may evolve with time. Specifically, the instrumental intensity is continuously predicted from the vertical  $P_x$  amplitude and, by definition of the  $P_x$  parameter, it can only increase or remain stable with time, so that once the predicted intensity has exceeded the threshold for warning declaration, the alert cannot be cancelled. With this in mind, the prediction performance at any recording sites may potentially evolve with time from SNA (light green) to FA (yellow) or from MA (red) to SA (dark green). Other transitions between alert states are, de facto, not possible.

Indeed, initial PGV underestimations leading to MA and SNA can be related to P-window lengths shorter than the half-duration of the earthquake source time function (Colombelli and Zollo [2015]) resulting in an initial magnitude underestimation. As the P-window time increases, since the max P-peak amplitude can only increase, the MAs can be confirmed or evolve in Successful Alerts, if the predicted PGV becomes larger than the threshold.

On the other hand, SNAs can be confirmed or, if the predicted PGV increases, can only evolve in False Alerts. With similar arguments, we note that, since the predicted PGV can only increase with an enlarged P-window, both all SAs and FAs would not change their status.

Building an EEW system that evolves with time in a manner that missed alerts and successful no-alerts tend to be minimized while increasing the number of successful alerts represent a strong advantage of the proposed EEW method, although this result is achieved at the expenses of an increase of false alerts. A similar conclusion was drawn by Minson *et al.* [2021] who analyzed the ideal case of a rail system in California's San Francisco Bay Area to explore potential uses of a network-based EEW system for rail systems.

With this regard, we note that, at the first alert time and after, the relative percentage of SA, SNA, FA and MA critically depends on the predicted PGV (through the measured  $P_x$  (eq.4)) and on the chosen IMM (or PGV) threshold, due to the natural distribution and scattering of data around the empirical laws that are used to predict PGV from the P-peak amplitude. This is clearly depicted in



Figure 6, that shows an example of the used empirical attenuation relations between PGV and  $P_v$ . For a given PGV threshold and a measured value of  $P_v$ , the diagram Predicted PGV vs measured P-amplitude is partitioned in 4 regions, around the predicted PGV point: the regions of SAs (dark-green, top-right), SNAs (light-green, bottom-left), FA (yellow, bottom-right) and MA (red, top-left). It is clear how the relative proportion of SA, SNA, FA and MA depends on the measured  $P_x$  and selected PGV threshold, that can change with time as the  $P_x$  value and associated predicted PGV increase. This example demonstrates that if PGV's predictions are based on empirical regressions of P-wave amplitude data, the optimal future solution to improve the performance of the time-evolutive EEW system is to refine and make more robust the empirical PGV prediction laws. This will be possibly achieved using AI-based machine learning approaches or through the exploration of more complex multi-parametric regression models (which includes site, azimuthal, distance effects) than the ones represented by eqs. 4.

## **Conclusions**

We have proposed an EEW method which uses the real-time P-peak amplitudes progressively measured at a dense accelerometric network around the epicenter to track the time-evolving potential damage zone, i.e the area within which the strong ground motion is expected to exceed a given instrumental intensity threshold. Compared with source-based early warning approaches, where the event magnitude and location are used to issue an alert, our method follows a shaking-forecast-based strategy, where the alert is rather issued upon the prediction of the strong ground shaking amplitudes at sites to be secured during the earthquake emergency. The method is time-evolutive, since the shape of the potential damage zone is modeled according to new data incoming from progressively distant stations and larger P-wave windows are assimilated by the EEW system. The potential damage zone is traced by combining the Peak Ground Velocity values predicted by early P-wave amplitudes at accelerometer sites with values predicted by the regional GMPE using the updated values of location and moment magnitude.

We showed that the P-wave-based, early shake-map well reproduce the elongation and shape of the final shake-map and the extent of the area driven by the rupture directivity and that suffered the largest shaking and damage during the October 30, 2016, M 6.5 Central Italy event.

The offline simulation of the EEW method illustrates a common characteristic of time-evolutive systems, i.e. while trying to reduce uncertainties as much as possible, it will not be possible to eliminate the occurrence of false and missed alarms, so it is necessary for the end-user to accept these eventualities and account for them in a probabilistic frame to be implemented in a user-specific, decision-making strategy for minimizing the earthquake impact in real-time.

Despite these intrinsic limitations, a time-evolutive EEW as the one illustrated in our study, can help to implement strategies to mitigate the earthquake impact on false alert-tolerant users, who set the threshold and time of the alerts based on their specific risk mitigation actions, thus averaging between the requirement of the system to be fast in alerting (long lead-times) and accurate in the shaking predictions (reduced number of missed and false alarms).

## **Acknowledgements**

The authors thank the members of the Early Warning Group at the Seismological Laboratory (RISSCLAB) of the Department of Physics of the University of Naples Federico II, for their support and contribution of ideas during the research development. The research has been partially funded by :

- the Italian Ministry of University and Research (MUR) through the National Operative Programme (PON-AIM 218 AIM1834927 – 3) and the project European Plate Observing System (EPOS)-Italia
- the Department of Civil Protection (DPC), through a research contract with the University of Naples Federico II

## **Conflict of interest**

The authors declare no conflicts of interest relevant to this study

## **Data Availability Statement**

All of the data used to undertake this research are freely available. The specific source for the data is provided in the text and summarized below.

- Strong-motion records of the Mw 6.5, October 30, 2016 Norcia (Central Italy) earthquake acquired by the Italian Accelerometric Network (RAN) owned by the Department of Civil Protection – ITACA V3.2 Waveform DataBase available at <https://itaca.mi.ingv.it/>

## **References**

- Alcik, H., Ozel, O., Apaydin, N., Erdik, M., 2009. A study on warning algorithms for Istanbul earthquake early warning system. *Geophys. Res. Lett.* 36, L00B05.  
<https://doi.org/10.1029/2008GL036659>
- Allen, R.M., Melgar, D., 2019. Earthquake Early Warning: Advances, Scientific Challenges, and Societal Needs. *Annu. Rev. Earth Planet. Sci.* 47, 361–388. <https://doi.org/10.1146/annurev-earth-053018-060457>
- Allen, R. M., and A. Ziv (2011), Application of real-time GPS to earthquake early warning, *Geophys. Res. Lett.*, 38, L16310, doi:10.1029/2011GL047947
- Allen RM, Gasparini P, Kamigaichi O, Böse M. 2009. The status of earthquake early warning around the world: an introductory overview. *Seismol. Res. Lett.* 80(5):682–93
- Bindi, D., Pacor, F., Luzi, L., Puglia, R., Massa, M., Ameri, G. and R. Paolucci (2011) Ground motion prediction equations derived from the Italian strong motion database. *Bull Earthquake Eng* (2011) 9:1899–1920, DOI 10.1007/s10518-011-9313-z
- Boore, David & Stephens, Chris & Joyner, William. (2002). Comments on baseline correction of digital strong-motion data: examples from the 1999 Hector Mine, California, earthquake. *Bulletin*

of the Seismological Society of America. 92. 1543-1560.

Böse, M., Thomas H. Heaton, Egill Hauksson (2012) Real-time Finite Fault Rupture Detector

(FinDer) for large earthquakes, *Geophysical Journal International*, Volume 191, Issue 2, November,

Pages 803–812, <https://doi.org/10.1111/j.1365-246X.2012.05657.x>

Caruso, A., S. Colombelli, L. Elia, M. Picozzi and A. Zollo, (2017) An onsite alert level early warning

system for Italy, *J. Geophys. Res. Solid Earth*, 122, doi 10.1002/2016JB01340Cheloni, D., et al.

(2017), Geodetic model of the 2016 Central Italy earthquake sequence inferred from InSAR and

GPS data, *Geophys. Res. Lett.*, 44, 6778–6787, doi:10.1002/2017GL073580

Colombelli, S., Zollo, A., Festa, G., and Kanamori, H. (2012), Early magnitude and potential damage

zone estimates for the great Mw 9 Tohoku-Oki earthquake, *Geophys. Res. Lett.*, 39, L22306,

doi:[10.1029/2012GL053923](https://doi.org/10.1029/2012GL053923).

Colombelli, S., R. M. Allen, and A. Zollo (2013), Application of real-time GPS to earthquake early

warning in subduction and strike-slip environments, *J. Geophys. Res. Solid Earth*, 118,

doi:10.1002/jgrb.50242

Colombelli, S., A. Zollo, G. Festa, and M. Picozzi (2014), Evidence for a difference in rupture

initiation between small and large earthquakes, *Nat. Commun.*, 5, 3958,

doi:10.1038/ncomms4958.

Colombelli, S., Caruso, A., Zollo, A., Festa, G. and Kanamori, H. (2015), A P wave-based, on-site

method for earthquake early warning. *Geophys. Res. Lett.*, 42: 1390– 1398. doi:

10.1002/2014GL063002

Colombelli, S., and A. Zollo (2015) Fast determination of earthquake magnitude and fault extent

from real-time P-wave recordings, *Geophysical Journal International*, Volume 202, Issue 2, , Pages

1158–1163, <https://doi.org/10.1093/gji/ggv217>

Colombelli, Simona & Festa, Gaetano & Zollo, Aldo. (2020). Early rupture signals predict the final

earthquake size. *Geophysical Journal International*. 223. 692-706. 10.1093/gji/ggaa343.

- Clinton J, Zollo A, Marmureanu A, Zulfikar C, Parolai S. 2016. State-of-the art and future of earthquake early warning in the European region. *Bull. Earthq. Eng.* 14(9):2441–58
- Faenza L. and A. Michelini, (2010). Regression analysis of MCS intensity and ground motion parameters in Italy and its application in ShakeMap, *Geophysical Journal International*, Volume 180, Issue 3, March 2010, Pages 1138–1152, <https://doi.org/10.1111/j.1365-246X.2009.04467.x>
- Gruppo di Lavoro INGV sul terremoto in centro Italia (2016). Rapporto di sintesi sul Terremoto in centro Italia Mw 6.5 del 30 ottobre 2016, doi: 10.5281/zenodo.166019 (in Italian).
- Grapenthin, R., Johanson, I. A., and Allen, R. M. (2014), Operational real-time GPS-enhanced earthquake early warning, *J. Geophys. Res. Solid Earth*, 119, 7944– 7965, doi:10.1002/2014JB011400.
- Kanamori H. Real-time seismology and earthquake damage mitigation. *Ann Rev Earth Planet Sci* 2005;33:195–214, doi:10.1146/annurev.earth. 33.092203.122626.
- Kodera, Y., Yasuyuki Yamada, Kazuyuki Hirano, Koji Tamaribuchi, Shimpei Adachi, Naoki Hayashimoto, Masahiko Morimoto, Masaki Nakamura, Mitsuyuki Hoshiba (2018) The Propagation of Local Undamped Motion (PLUM) Method: A Simple and Robust Seismic Wavefield Estimation Approach for Earthquake Early Warning. *Bulletin of the Seismological Society of America* , 108 (2): 983–1003. doi: <https://doi.org/10.1785/0120170085>
- Lomax, A., J. Virieux, P. Volant and C. Berge, 2000. Probabilistic earthquake location in 3D and layered models: Introduction of a Metropolis-Gibbs method and comparison with linear locations, in *Advances in Seismic Event Location* Thurber, C.H., and N. Rabinowitz (eds.), Kluwer, Amsterdam, 101-134..
- Lomax, A., C. Satriano and M. Vassallo (2012), Automatic picker developments and optimization: FilterPicker - a robust, broadband picker for real-time seismic monitoring and earthquake early-warning, *Seism. Res. Lett.* , 83, 531-540, doi: 10.1785/gssrl.83.3.531
- Luzi L., Puglia R, Russo E & ORFEUS WG5 (2016). Engineering Strong Motion Database, version 1.0.

- 712 Istituto Nazionale di Geofisica e Vulcanologia, Observatories & Research Facilities for European  
713 Seismology. doi: 10.13127/ESM
- 714 Minson, S.E., Baltay, A.S., Cochran, E.S. et al. The Limits of Earthquake Early Warning Accuracy and  
715 Best Alerting Strategy. Sci Rep 9, 2478 (2019). <https://doi.org/10.1038/s41598-019-39384-y>
- 716 Nakamura Y, Tucker BE. 1988. Japan's earthquake warning system: should it be imported to  
717 California? Calif. Geol. 41(2):33–40
- 718 Minson, S.E., Cochran, E.S., Wu, S., Noda, S. (2021). A Framework for Evaluating Earthquake Early  
719 Warning for an Infrastructure Network: An Idealized Case Study of a Northern California Rail  
720 System. Front. Earth Sci. 9, 620467. <https://doi.org/10.3389/feart.2021.620467> Nazeri, S.,  
721 Colombelli, S. & Zollo, A. (2019), "Fast and accurate determination of earthquake moment, rupture  
722 length and stress release for the 2016-2017 Central Italy seismic sequence", Geophysical Journal  
723 International, Volume 217, Issue 2, Pages 1425–1432, doi.org/10.1093/gji/ggz097
- 724 Odaka, T., K. Ashiya, S. Tsukada, S. Sato, K. Ohtake, and D. Nozaka (2003). A new method of quickly  
725 estimating epicentral distance and magnitude from a single seismic record. Bulletin of the  
726 Seismological Society of America 93, 526–532.
- 727 Scognamiglio, L., Tinti, E., Casarotti, E., Pucci, S., Villani, F., Cocco, M., et al. (2018). Complex fault  
728 geometry and rupture dynamics of the MW 6.5, 30 October 2016, central Italy earthquake. Journal  
729 of Geophysical Research: Solid Earth, 123, 2943– 2964. <https://doi.org/10.1002/2018JB015603>
- 730 Satriano, C., Lomax, A., Zollo, A. (2008). Real-Time Evolutionary Earthquake Location for Seismic  
731 Early Warning. Bulletin of the Seismological Society of America, 98 (3): 1482–1494.  
732 <https://doi.org/10.1785/0120060159>
- 733 Trugman, D. T., Page, M. T., Minson, S. E., & Cochran, E. S. ( 2019). Peak ground displacement  
734 saturates exactly when expected: Implications for earthquake early warning. Journal of  
735 Geophysical Research: Solid Earth, 124, 4642– 4653. <https://doi.org/10.1029/2018JB017093>
- 736 Yamamoto, S., Rydelek, P., Horiuchi, S., Wu, C., and Nakamura, H. (2008), On the estimation of

seismic intensity in earthquake early warning systems, *Geophys. Res. Lett.*, 35, L07302,

doi:[10.1029/2007GL033034](https://doi.org/10.1029/2007GL033034).

Wald, D. J., C. B. Worden, V. Quitoriano, and K. L. Pankow (2006). ShakeMap® Manual,

Technical Manual, Users Guide, and Software Guide;

<http://pubs.usgs.gov/tm/2005/12A01/pdf/508TM12-A1.pdf>.

Worden, C. B., Wald, D. J., Allen, T. I., Lin, K. Garcia, D. and G. Cua; A Revised Ground-Motion and

Intensity Interpolation Scheme for ShakeMap (2010) *Bulletin of the Seismological Society of*

*America* 100 (6): 3083–3096. doi: <https://doi.org/10.1785/0120100101>

Wu, Y. M., and H. Kanamori (2005), Experiment of an on-site method for the Taiwan Early Warning

System, *Bull. Seismol. Soc. Am.*, 95, 347–353, doi:10.1785/0120040097

Wu, Y.-M., and L. Zhao (2006), Magnitude estimation using the first three seconds P-wave

amplitude in earthquake early warning, *Geophys. Res. Lett.*, 33, L16312,

doi:10.1029/2006GL026871

Zollo, A., Amoroso, O., Lancieri, M., Wu, Y. And H. Kanamori (2010). A Threshold-based

Earthquake Early Warning using dense accelerometer networks. *Geophysical Journal International*.

183. 10.1111/j.1365-246X.2010.04765.x.

Zollo, A., Lancieri, M. & Nielsen, S. (2006) Earthquake magnitude estimation from peak amplitudes

of very early seismic signals on strong motion. *Geophys. Res. Lett.* 33, L23312,

<https://doi.org/10.1029/2006GL027795> (2006)

Zollo, A., Nazeri, S. and S. Colombelli, (2021a) Earthquake Seismic Moment, Rupture Radius, and

Stress Drop From P-Wave Displacement Amplitude Versus Time Curves, *IEEE Transactions on*

*Geoscience and Remote Sensing*, vol. 60, pp. 1-11, 2022, Art no. 5912211, doi:

10.1109/TGRS.2021.3119909.

Zollo, A., Caruso, A., De Landro, G., Colombelli, S., & Elia, L. (2021b). A Bayesian method for real-time earthquake location using multiparameter data. *Journal of Geophysical Research: Solid Earth*, 126, e2020JB020359. <https://doi.org/10.1029/2020JB020359>

#### Figure Captions

**Figure 1: Block Diagram of the method.** The figure shows the block diagram of the methodology, in which on-site PGV predictions (left) are combined with network-based PGV predictions (center), for a refined, real-time shake map construction and dissemination of alerts at target sites (right).

**Figure 2: Example of seismogram and LPDT curves .** a) Examples of acceleration records at increasing distance from the source (from top to bottom). Colors are used to identify the corresponding stations in panels b) and c) and for each station, the hypocentral distance is reported on the plot. b) LPDT curves computed at each station, starting at the P-wave arrival (shown with a coloured circle on each seismogram) and stooping at the expected arrival of S-waves. For a matter of visualization, the LPDT curves are initialized to a common, amplitude value. c) Map of the epicentral position of the earthquake and recording stations within a maximum distance of 50 km.

**Figure 3: Time evolutive estimation of event location and magnitude.** The plot shows the comparison between the real-time earthquake location (top panel) with the bulletin solution, both for the epicentral position (black line) and for the earthquake depth (grey line). The bottom panel shown the real-time estimate of the earthquake magnitude, as average values (gray circles) and their uncertainties (error bars). Magnitude estimates form available agencies are also shown for reference, with horizontal lines. In both panels, the x-axis shows time in seconds form the origin



time of the event.

**Figure 4: Result for the 2016-10-30 Mw6.5 Norcia (Italy) earthquake.** Examples of the evolutionary, P-wave based early shake maps at different seconds from origin time (reported in each panel). In each panel, stations are the gray triangles, the red star is the epicenter of the event and the contour lines for the predicted intensity levels VII and VIII are also shown. The bottom-right panel is the reference INGV shake map.

**Figure 5: Performance Evaluation.** The figure shows the performance of the system at the three different times in terms of Successful Alerts (dark green), Successful No-Alerts (light green), Missed Alerts (red) and False Alerts (yellow) at each station position. In all panels, the yellow circle is the 40km radius around the epicenter, while the red circle represents the blind zone.

**Figure 6: Lead-Time map.** The figure shows values the map of available lead-times in the epicentral area and the position of municipalities that could have benefit from the warning. Each circle on the map represents the area in which the corresponding lead-time (indicated in white) would have been available.

Figure1.

### 3-Component Waveforms (Real-time or Playback)

Parameters

Regression Laws

INPUTS

*Time-Varying Mapping  
of Peak Ground Shaking  
BLOCK DIAGRAM*

IN

#### ON-SITE PROCESSING

1. P-waves Arrival  
[ FilterPicker ]

2. Waveform Quality & Filter  
Selection [ SAVE ]

3. Log(Pv) vs. Time Curve  
[ LPDT: Plateau Reached? ]

4. PGV Prediction ON-SITE  
[ PGV(Pd,Pv,Pa) from  
P-waves / Vertical ]

5. PGV Measure  
[ from P/S-waves / Horizontals ]

PICKS

$P_x$  Peak  
At Plateau

$PGV_{ONSITE} =$   
 $\max(PGV_{PRED}, PGV_{MEAS})$

#### NETWORK-BASED PROCESSING

1. Location  
[ M-PLOC: Differential Pick Times  
+ (optional) Pv ratios + (optional) Back-Azimuths ]

2. Magnitude  
[ weighted average of stations  
 $M(P_d, R)$ ,  $M(P_v, R)$ ,  $M(P_a, R)$  at Plateau ]

3. PGV prediction from GMPE (Loc., Mag.)

PGV

GMPE

4. ShakeMap (Worden et al.)  
[ P-waves + S-waves + GMPE ]

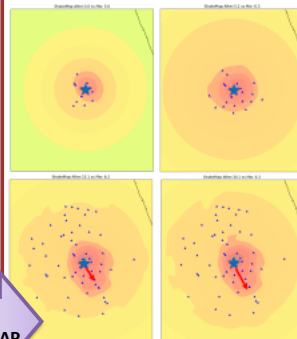
PGV

SHAKEMAP

PGV

ONSITE

#### REAL TIME PEAK GROUND SHAKING INTERPOLATION



OUT

OUTPUTS

Alerts to  
Specific Targets

Figure2.

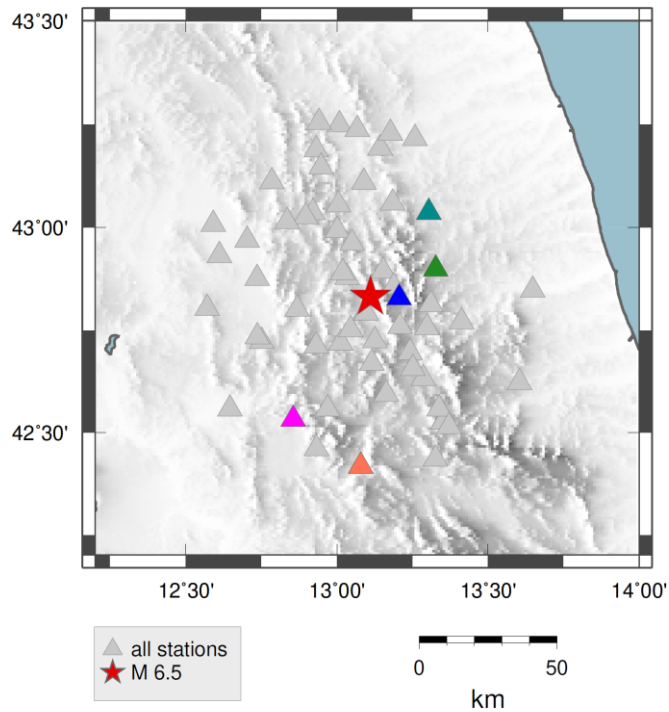
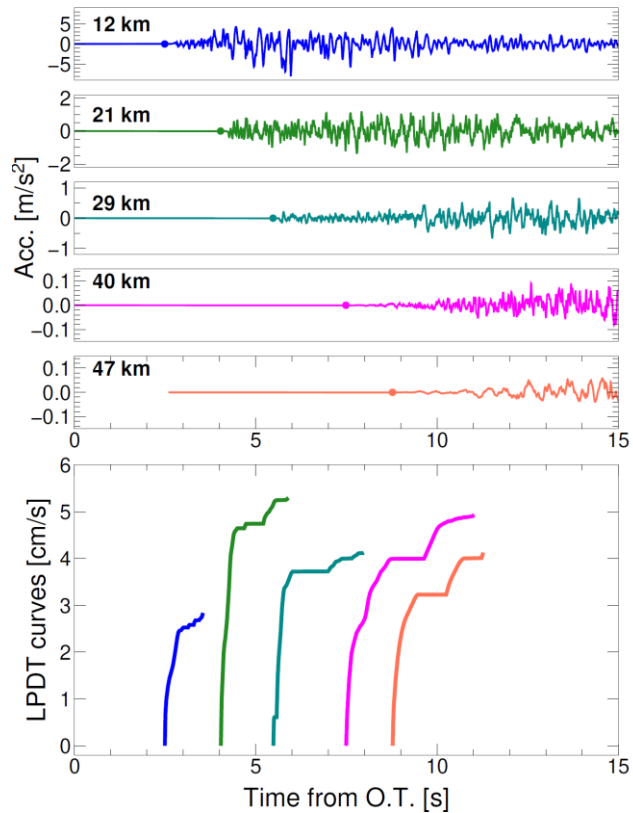


Figure3.

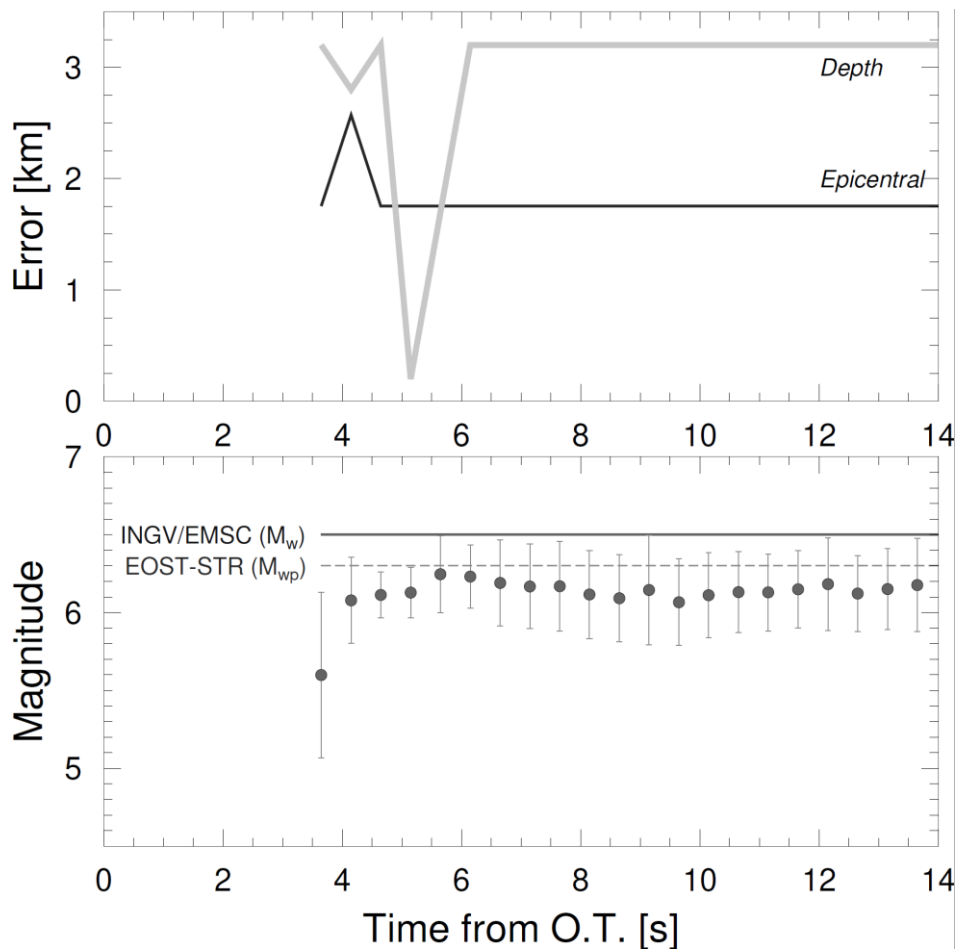
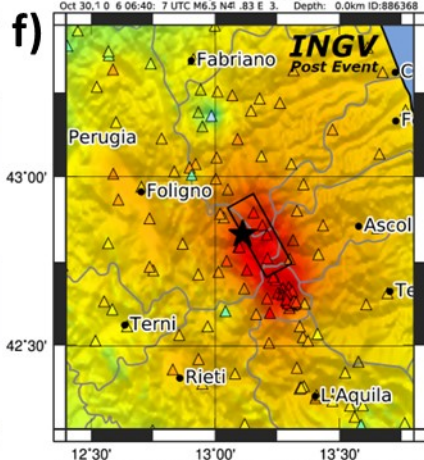
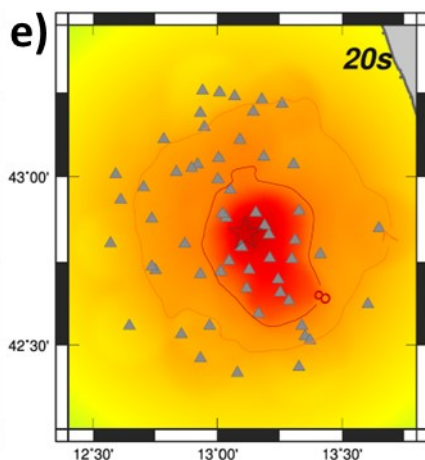
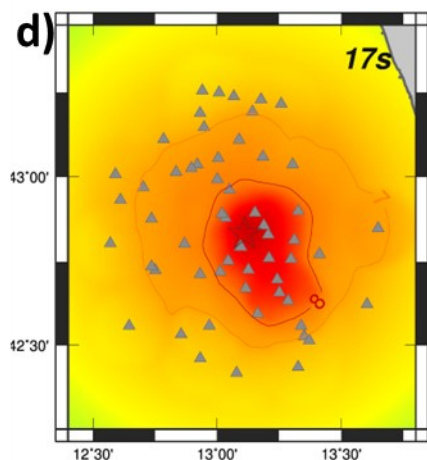
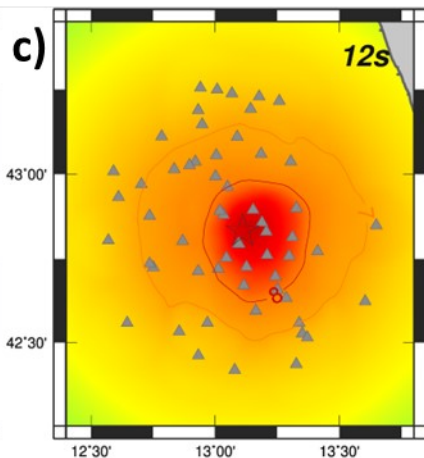
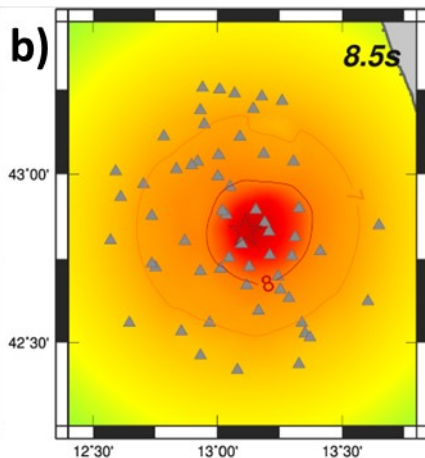
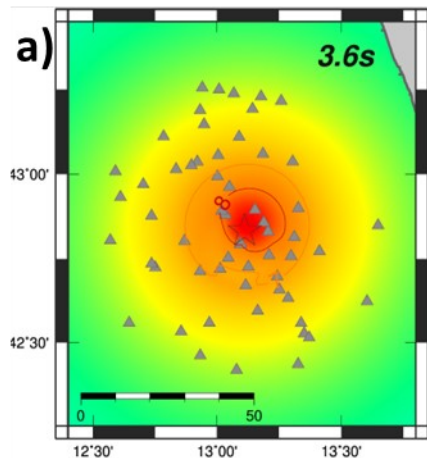


Figure4.





Macroseismic Intensity Map INGV  
ShakeMap: 4 km NE Norcia (PG)  
Oct 30.10 6 06:40 7 UTC M6.5 N46.83 E 3. Depth: 0.0km ID:886368

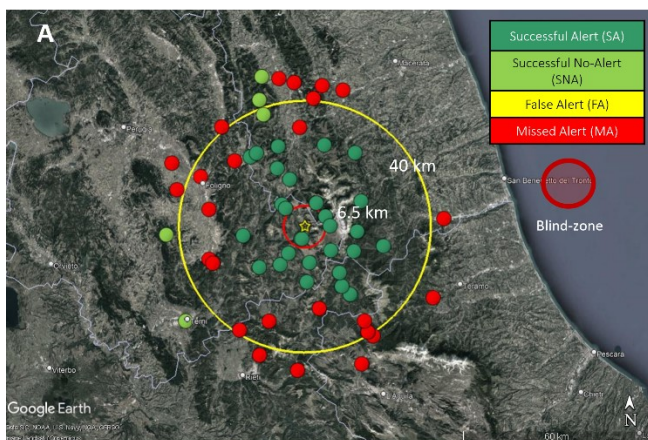
SHAKING	Not felt	Weak	Light	Moderate	Strong	Very strong	Severe	Violent	Extreme
DAMAGE	None	None	None	Very light	Light	Moderate	Moderate/heavy	Heavy	Very heavy
PERMANENT DISPLACEMENT	0.0	0.0	0.0	0.0	0.0	0.0	0.0	0.0	0.0
PERMANENT DISPLACEMENT	0.0	0.0	0.0	0.0	0.0	0.0	0.0	0.0	0.0
INTENSITY	I	II	III	IV	V	VI	VII	VIII	IX

Scale based on Fattori and Meisner (2010) 0.5-1.0 1.0-1.5 1.5-2.0 2.0-2.5 2.5-3.0 3.0-3.5 3.5-4.0 4.0-4.5 4.5-5.0 5.0-5.5

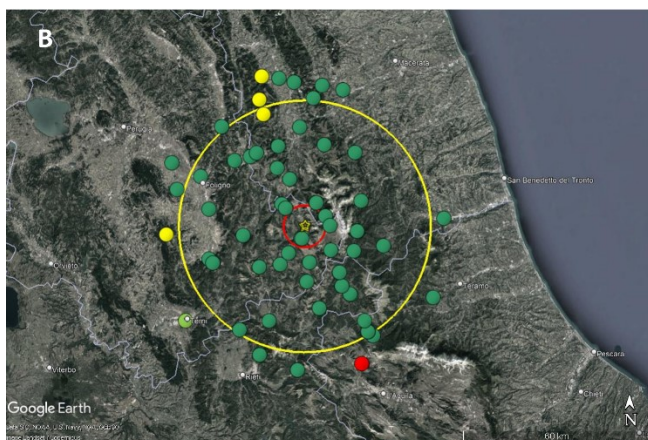
0.5 Seismic Instrument 1 Reported Intensity ★ Epicenter □ Rupture

Figure5.

Time TFA=3.65 sec since OT



Time 4.15 sec since OT



Time 5.15 sec since OT

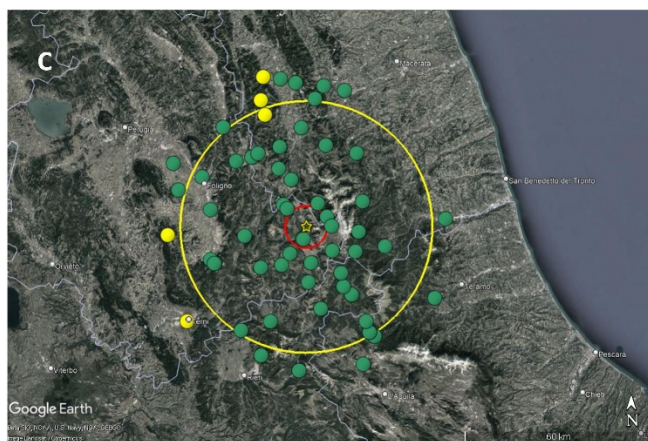


Figure6.



